ORIGINAL RESEARCH ARTICLE

The Stress-Controlled Low Cycle Fatigue Properties of HK40 and HP40 Heat-Resistant Fe–Ni Base Alloys

ZHUO LIU and SAMMY TIN

The low cycle fatigue (LCF) properties of centrifugally cast Centralloy ET 45 MICRO (HK40 type) and Centralloy G 4852 MICRO (HP40 type) were quantified using fully reversed, stress-controlled fatigue tests at temperatures between 350 °C and 600 °C. Cast samples for both alloys were artificially aged to simulate the microstructure of alloys observed during service before assessing the LCF properties. Despite having a similar yield strength, the Centralloy ET 45 MICRO alloy was measured to exhibit reduced LCF properties when compared to Centralloy G 4852 MICRO specimen at elevated temperatures. The differences are largely attributed to variations in the size distribution of the primary Cr carbide clusters resulting from the solidification conditions. The ratio of stress amplitude over yield strength shows good agreement with the lifetime at every tested temperature as $\frac{\sigma_a}{\sigma_Y} = A\left(N_f\right)^C$. At elevated temperatures and high stress amplitudes, plastic deformation and stress relaxation contribute to improving the overall LCF properties of both alloys. However, at smaller stress amplitudes where the test times are prolonged, elevated temperatures are responsible for deteriorating the LCF response of the alloys.

I. INTRODUCTION

THE HK40 type material (such as Centralloy ET 45 MICRO[1]) and HP40 type material (such as Centralloy G 4852 MICRO[2]) are cast austenitic heat-resistant alloys that are commonly utilized as key structures that need to endure hydrocarbon and steam environments at elevated temperature for over 100,000 hours. These alloys are crucial for supporting the design of a variety of structures used for power generation or in the chemical and petrol-chemical processing industry. The high Cr in the Ni–Cr–Fe–Si matrix in conjunction with the primary carbides distributed throughout the microstructure provides this class of alloys with good resistance to high temperature corrosion, creep, and microstructural stability. The intergranular primary carbides or carbo-nitrides and the Cr-rich intergranular carbides greatly affect the generation of good high temperature properties during service. Secondary carbides often precipitate from the matrix during service and contribute significantly to strengthening as they impede the dislocation movement at elevated temperature. It has also been reported that the primary NbC carbides can transform into Ni–Nb–Si-rich G phase ($Nb_6 Ni_{16}Si_7$) during long-term exposure to service temperatures, which contributes to reducing the overall ductility of the alloy.[3–5] The mechanical properties under uniaxial loading at elevated temperature of these two materials have been well established.[1,2,6–11] However, the fatigue properties at elevated temperatures of these alloys have not been addressed in detail.[10,11]

Fatigue is the most common mode of failure for many engineering structures. It is critical to have a sufficient understanding of the characteristic fatigue properties of materials under complex working conditions to ensure the safety and reliability. Fatigue occurs when materials are subjected to repeated loading and unloading cycles over and the behavior is influenced by several factors including the loading mode, the magnitude and frequency of loading, the service environment, and the microstructure of the material.[12] The formation of fatigue cracks is one of the primary damage mechanisms leading to failure. The initiation of the fatigue cracks tends to occur in regions of the microstructure where localized stress concentrations caused by dislocation pile-up[13,14] form, and the subsequent crack growth can accelerate the degradation of mechanical properties of the material. The fatigue properties of materials can be evaluated using a variety of methods that aim to simulate the actual service conditions under which the

ZHUO LIU is with the Illinois Institute of Technology, 10 W, 32nd Street, Chicago, IL 60616. Contact e-mail: zliu110@hawk.iit.edu SAMMY TIN is with the University of Arizona, 1235 E. James E. Rogers Way, Mines Bldg. 131, Tucson, AZ 85721.

structures operate. One important characteristic of fatigue behavior is the fatigue lifetime, defined as the number of cycles to failure (N_f), comprising of both crack initiation and propagation until failure. In general, the fatigue properties are better when the material has a high yield strength. The grain size has great influence on fatigue properties as it impacts the manner in which dislocation accumulation occurs and also impacts the ability of cracks to grow during cyclic loading conditions.[15,16] Moreover, intrinsic defects such as cracks, porosity, and inclusions in the microstructure of the material can act as fatigue crack initiation sites leading to the fatigue failure.[12,17–19] The crack initiation at large-grained materials and microstructures containing hard particles such as carbide particles has been studied with the comparison of the grain size and the inclusion size of the material.[20] The environment surrounding the material, such as the temperature and the corrosiveness, may also influence the fatigue properties of the material. Generally, for metallic materials, the fatigue lifetime is sensitive to temperature with lower temperatures being desired due to the higher yield strength. In addition, elevated temperatures may promote the diffusion and segregation of impurities along grain boundaries and surface-connected cracks to accelerate crack propagation.[12,21]

Low cycle fatigue (LCF) is caused by the accumulation of plastic deformation. It typically occurs in the materials subjected to high stress amplitudes and low loading frequencies, resulting in large strain variations and a high crack growth rate, respectively.[12,22–24] In real life, structural components are designed such that they can survive repeated cyclic loading conditions when subjected with loads exceeding the elastic limit of its material. This commonly occurs along regions where stress concentrations are present or when structures are subjected to large thermal cycles that result in thermal strains that result in localized yielding of the material. Repeated thermal cycling induces expansion and contraction events that can lead to crack initiation and growth. In addition, associated with LCF effect, other damage mechanisms are operative in the material at elevated temperature during cyclic loading, such as creep-fatigue[25–28] or stress relaxation at the crack tip.[29–31] Understanding the LCF performance of the material is also the foundation of establishment of the thermo-mechanical fatigue (TMF) properties under complicated service conditions.

Strain-controlled or stress-controlled fatigue tests are common methods to evaluate the LCF properties of structural materials. Strain-controlled LCF has advantages in understanding the effect of strain on the fatigue properties of the material and the lifetime can be predicted following the Manson–Coffin equation.[32] However, the stress-controlled LCF can often provide a better representation of the cyclic loading conditions experienced under actual service because most structures are designed for stress-controlled cycling, rather than strain-controlled. It has been reported in some literature that the stress-controlled LCF lifetime is much smaller than the strain-controlled one.[33,34] However, most investigations utilize strain control for reporting LCF

properties of material, while stress-control is used for reporting the high cycle fatigue properties of materials.

With the need to establish safe operating practices during long-term service in harsh, high-temperature environments, the LCF properties of materials need to be quantified to understand how damage accumulates and develop predictive safe-life criterion for removing and servicing materials before catastrophic failure. The goal of the current study is to investigate the LCF properties of centrifugal casting Centralloy ET 45 MICRO and Centralloy G 4852 MICRO at elevated temperatures in the version of "stress versus lifetime" and figure out the influences on the LCF properties at elevated temperature.

II. MATERIAL AND EXPERIMENTAL PROCEDURE

A. *Fatigue Test Specimen Preparation*

In this experiment, the Centralloy ET 45 MICRO (Ni–0.45C–1.6Si–1Mn–35Cr–16Fe−1Nb, wt pct) was referred to as 3545 specimen and the Centralloy G 4852 MICRO (Ni–0.45C–1.5Si–1Mn–25Cr–35.55Fe−1.5Nb, wt pct) was referred to as 2535 specimen. The alloys were centrifugally cast into pipes with varying wall thicknesses of about 13.97 and 7.62 mm for 3545 and 2535, respectively, as shown in Figure 1(a). During prolonged service at elevated temperatures, the as-cast microstructures of these alloys evolve and various carbide precipitates within the material to provide precipitation strengthening. To assess the fatigue properties of the material in the precipitation hardened condition, heat treatments were employed to artificially age the microstructures prior to fatigue testing. The 3545 specimen was heat treated at 800 °C for 200 hours and the 2535 specimen was heat treated at 850 °C for 500 hours, followed by furnace-cooling. The heat treatment procedure was selected based on the understanding of the service conditions and environments of these material to induce phase change. Mechanical test specimens were obtained by sectioning the pipes axially into cylindrical blanks using wire electrical discharge machining. The diameters of the bar specimens were maximized given the thickness of the pipe wall. The fatigue specimens were then CNC-machined to make standard fatigue specimens with a reduced diameter and curvature surface, as shown in Figure 1(b). Before the fatigue test, the surface of the reduced section of the specimens was polished using 120, 320, 400, and 600 grit grinding paper to remove all surface imperfections and machining marks.

B. *Fatigue Test Set-Up*

The symmetric, fully reversed stress-controlled fatigue tests were operated using an MTS servo-hydraulic test machine with a frequency of 1 Hz with applied stress ranging between 480 and 300 MPa and temperatures ranging between 600 °C and 350 °C. Induction heating was used to attain the desired test temperatures, and
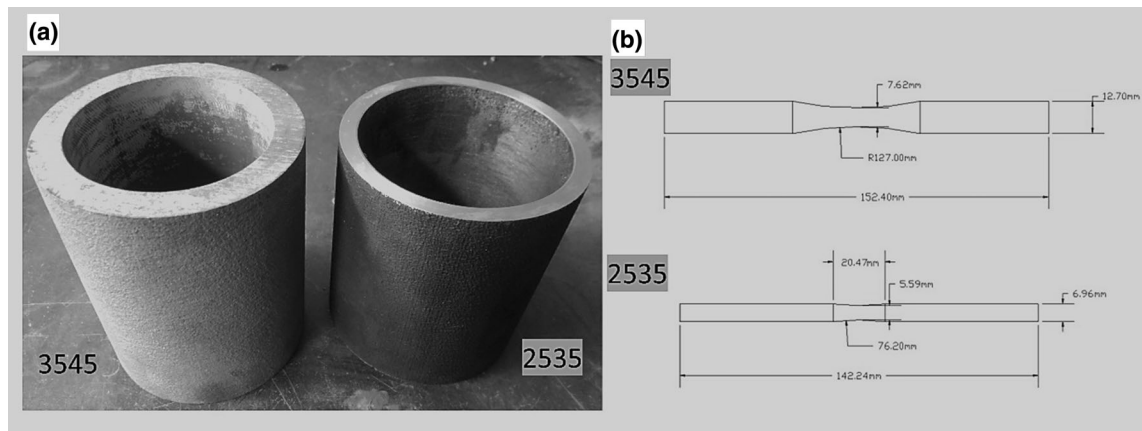
Fig. 1—(a) The centrifugal cast 3545 specimen (wall thickness about 13.97 mm) and 2535 specimen (wall thickness about 7.62 mm). (b) The fatigue test specimen dimension. The specimens were sectioned to the largest diameter against the pipe wall.

temperatures of the specimen were controlled with a thermocouple attached on the shoulder of the test specimen. The load was maintained at zero during the heating procedure. After the testing temperature was achieved, the specimens were soaked for 5 minutes, and an independent infrared temperature sensor was used to measure and monitor the temperature at the middle of the reduced section to ensure the specimen temperature was maintained at the desired testing temperature with an error less than 5 °C. For each test condition, three specimens were tested for each temperature and applied stress condition to assess the reproducibility of the results. The fatigue tests were conducted until fracture and the specimens were air-cooled to room temperature.

C. Microstructure Observation Analysis

Metallographic samples were prepared for observation using JEOL JSM 5900-LV scanning electron microscope (SEM) in the as-cast and heat-treated condition. Energy dispersive spectroscopy (EDS) using an Oxford Instruments X-Max system was utilized to measure the composition at an accelerating voltage of 20 kV. The low magnification microstructure was observed by an optical microscope on metallographic samples etched by Kalling's (5 g $CuCl_2$ + 50 mL HCl + 100 mL ethanol). Quantification of the microstructure was performed using ImageJ software on a minimum of ten SEM backscatter images and the results were averaged.

The grain structure was determined using an Oxford Instrument Nordlys-HKL electron backscatter diffractometer (EBSD) attached to the JEOL JSM 5900-LV SEM under 20 kV. A region of 1500 × 1200 μm^2 was mapped with a step size of 2.5 μm. Oxford Instruments Channel 5 software was used to analyze the data and generate the band contrast map that highlights grain boundaries.

III. RESULT

A. Microstructure Observation

Figure 2 shows the as-cast microstructures of 3545 and 2535 specimen before heat treatment. Both specimens exhibit dendritic features consisting of an austenitic matrix and a mixture of primary Cr carbides and NbC. However, the grain size of the two specimens is dramatically different. As shown in Figures 2(e) and (f), the microstructure scanned by EBSD is selected from the cross-section perpendicular to the longitudinal direction of the fatigue test specimen. The images reveal the differences in grain size between the 3545 and 2535, and also highlight the grain boundaries at the interface between different grain orientations. In these polycrystalline grain microstructures, the large grain sizes limit the number of overall grains that are able to be quantified, and therefore, the average grain size is difficult to be evaluated and compared. These results, however, clearly show that the grain size of the 3545 specimens is significantly larger than the 2535 specimens. This significant difference in grain size results from the solidification conditions associated with casting of the different pipe dimensions. Because the wall thickness of the 3545 casting is larger than 2535 raw material, the cooling rate of 3545 specimen during centrifugal casting is lower than the 2535 specimen. With a higher thermal gradient during solidification, the 2535 specimen has a higher nucleation rate for solidification but less time for growth. Therefore, both the grain size and characteristic dimensions of the dendritic features in the 2535 specimen are smaller than 3545 specimens.

During solidification, the primary carbides form along the interdendritic regions, as shown in backscatter SEM images in Figures 2(c) and (d). The phase marked as A is the primary Cr carbide cluster and B in lighter contrast represents the NbC.[3–5] The primary Cr carbides formed during solidification were reported as M_7C_3[35] in 3545 specimen and M_7C_3 with small amount
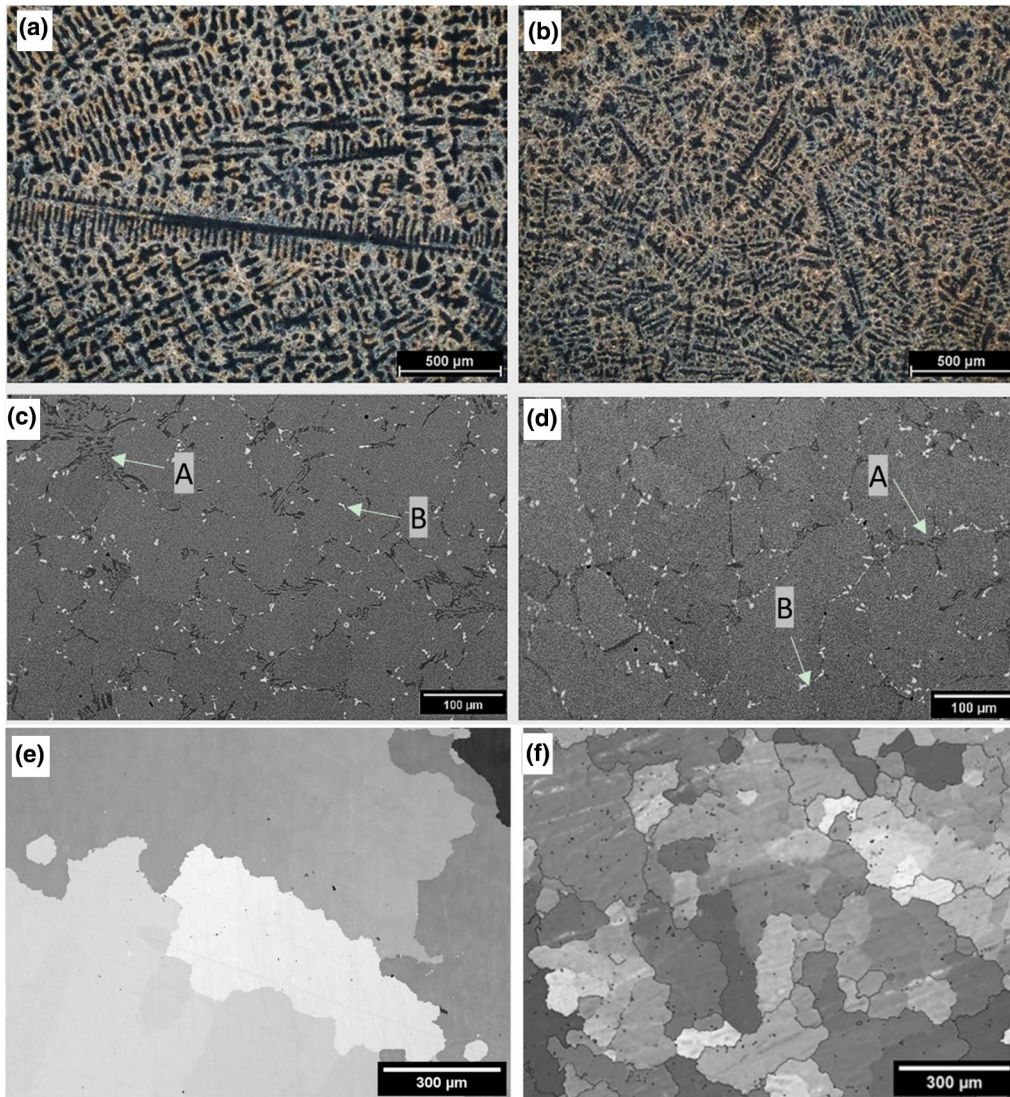
Fig. 2—(*a*) Optical dark-field images of the as-cast microstructure of 3545 specimen. (*b*) Optical dark-field images of the as-cast microstructure of 2535 specimen. (*c*) The as-cast microstructure of (c) 3545 specimen and (*d*) 2535 specimen imaged *via* backscattered SEM. The grain structure of (*e*) 3545 specimen and (*f*) 2535 specimen revealed by EBSD band contrast and grain boundary map. The mark A indicates the Cr-rich carbide cluster and B is the NbC.

of $M_{23}C_6$[8,36] in 2535 specimen. Although the level of carbon content in 3545 and 2535 specimen is similar, there is a noticeable difference in the primary carbides present in the two alloys. The fraction of primary carbides in the cast microstructure is listed in Table I. The area fraction of primary carbides in 3545 specimen is higher than 2535 specimen. A higher overall fraction of Cr carbides and less NbC are present in microstructure of the 3545 specimens than the 2535 specimens. The ratio of the fraction of NbC over Cr carbides is 0.25 in 3545 specimens and 0.44 in 2535 specimens. In addition, the carbide cluster (A) formed with a morphology consisting of thin, interconnected plate-like carbides in both specimens, but are more significant in 3545 specimens. The size of the clusters is related to the size of the interdendritic features and solidification rate. The blocky NbC carbides tend to remain as discrete particles, while the cluster of primary Cr carbides form an interconnected network of Cr carbides in the volume that are only apparent when the surrounding matrix is etched away. The area fraction of the cluster of carbides cannot be used to directly evaluate the actual size of the primary Cr carbides. Therefore, the size of the cluster was estimated using the largest measured length of each cluster of Cr carbides, which was measured as the longest distance that the carbide can cover in its region, as shown in Figures 3(a) and (b). The particle size distributions of the primary NbC and Cr carbide cluster for both alloys were measured, and the results are plotted in Figure 4. The average length of the clusters is 42 ± 3 μm for the 3545 specimens and 35 ± 5 μm for the 2535 specimens. The particle size distribution plots [Figure 4(a)] indicate the carbide clusters in the 3545 specimens have a larger distribution than 2535, as 2 pct of the primary carbide clusters were measured to be longer than 100 μm. The average size of the NbC

Table I. The Area Fraction of Primary Cr₇C₃ Carbide and NbC in the As-Cast 3545 and 2535 Specimens

Specimen	Cr Carbide (Percent)	NbC (Percent)	NbC/Cr Carbide	NbC + Cr Carbide (Percent)
3545	4.8 ± 0.1	1.2 ± 0.1	0.25	6
2535	3.9 ± 0.3	1.7 ± 0.1	0.44	5.6

carbides is shown in Figure 4(b), indicating that the 2535 specimen has a higher density of smaller NbC carbides than the 3545 specimen in the as-cast microstructure. In addition, some porosity also exists in the cast microstructure of 3545 and 2535 specimen, as highlighted in Figures 3(a) and (b). The sizes of the porosity tend to be smaller than that of the primary carbides and are heterogeneously distributed in the matrix.

The precipitates form during the initial heat treatment and modify the as-cast microstructure of the 3545 and 2535 specimens. As shown in Figure 5, a dispersion of dark precipitates form within the grain interior and along the interface between matrix and carbides in the 3545 specimen. From the EDS elemental distribution map, these intergranular precipitates are highly enriched with Cr, and are likely to be the secondary Cr carbides precipitates.[14] According to previous investigations,[3–5,36,37] the secondary carbide precipitates should be $M_{23}C_6$ carbides and the M_7C_3 carbides formed during solidification undergo the following transformation $M_7C_3 \rightarrow M_{23}C_6$ during long-term aging between 700 °C and 950 °C. Therefore, the Cr carbides that are present after heat treatment are likely to be a mixture of $Cr_7C_3/Cr_{23}C_6$. The heat treatment also serves to modify the phase stability of the NbC carbides, as the carbides decompose and become compositionally distinct. The EDS maps show that the carbides become surrounded by a lighter region consisting of Ni, Nb, and Si. This indicates that during the heat treatment, the Si solute atoms present in solution gradually diffuse across the NbC/matrix interface and transform the NbC into G phase, $Ni_{16}Si_7Nb_6$. From Figure 3, the NbC/G phase core–shell structure forms due to the slow diffusion of Si into the NbC. The transformation of NbC into G phase leads to a C and Nb release at the NbC/matrix interface, which result in the growth of an external G phase and $Cr_{23}C_6$. The diffusion of Nb through the G phase was identified as the limiting factor for the NbC dissolution, while the diffusion of Si from the matrix toward the precipitate is controlling the outward growth of the G phase.[3–5]

B. *The Yield Strength and LCF Fatigue Properties at Various Temperatures*

The stress–strain curves showing the yield strength measured at the 0.2 pct plastic strain offset of heat-treated specimens are shown in Figure 6. Experimentally measured values were compared with values reported from other published values[1,2,10], and the compiled results are listed in Table II. Compared with the reported yield strength of the alloys in the as-cast condition, the yield strength of both the 2535 and 3545

specimens is within 10 MPa following heat treatment. As temperature increases from 400 °C to 600 °C, the yield strength was observed to decrease by over 20 MPa in both specimens. Comparing the heat-treated 3545 specimens to 2535 specimens, the difference in yield strength at each temperature is within 20 MPa. The comparison of yield strength indicates that the 3545 specimens exhibit similar tensile properties with the 2535 specimen in the given temperature range. Extrapolating the effects of the temperature, the yield strength of heat-treated specimens at 450 °C and 350 °C was also estimated and is listed in Table II.

Stress-controlled fatigue tests were conducted at various temperatures for 3545 and 2535 under fully reversed loading conditions which means that the maximum tensile stress (σ_{max}) is equal to the magnitude of the maximum compressive stress (σ_{min}) but in opposite direction. In this case, the mean stress value during the test is zero and the stress ratio ($R = \sigma_{min}/\sigma_{max}$) is − 1. The stress amplitude (σ_a) is defined as shown in Eq. [1].

$$\sigma_a = \frac{\sigma_{max} - \sigma_{min}}{2} = \sigma_{max} \text{ as } \sigma_{max} = -\sigma_{min} \qquad [1]$$

The objective of this investigation was to understand the LCF behavior and ability of these materials to accommodate cyclic damage, so the stress amplitude and testing temperatures were selected to promote the fatigue fracture in the range from 10 to 5000 cycles. Figure 7 shows data plots of the stress amplitude versus the LCF lifetime of the heat-treated 3545 and 2535 specimens at various temperatures. The trendline of the stress amplitude over its yield strength at the corresponding testing temperature was also interpolated and is shown in Figure 8 and Table III. The 2535 specimens were observed to exhibit a longer lifetime from 350 °C to 600 °C at same stress amplitude or endured a higher applied stress amplitude than 3545 specimens within similar fatigue lifetime, as shown in Figures 7(a) through (e). This indicates that the 2535 specimens have better resistance to the LCF than the 3545 specimens at all selected testing temperatures.

To eliminate the influence of the differences in yield strength at various temperatures, the stress amplitude, σ_a, was divided by the yield strength (σ_Y) at the corresponding temperature. The ratio σ_a/σ_Y represents the influence of the maximum plastic strain during the fatigue tests. In Figure 8, generally, a linear relationship appears between the stress ratio and fatigue lifetime that corresponds to higher stress amplitudes being responsible for inducing fatigue failure to the shorter lives. The slope of the trendline gradually increases as the
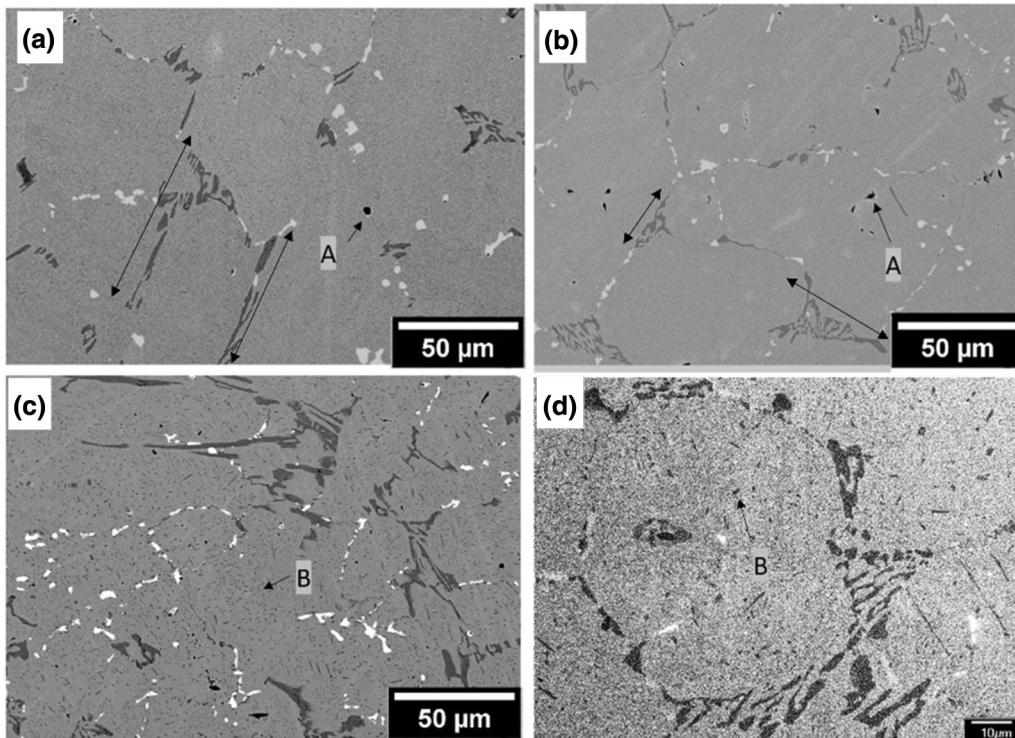
Fig. 3—The microstructure of as-cast (*a*) 3545 specimen, (*b*) as-cast 2535 specimen, (*c*) heat-treated 3545 specimen, and (*d*) heat-treated 2535 specimen. The region labeled with A represents the casting defect and B represents the Cr-rich precipitates generated during heat treatment. The measurement of Cr_7C_3 cluster length is shown in (a) and (b).
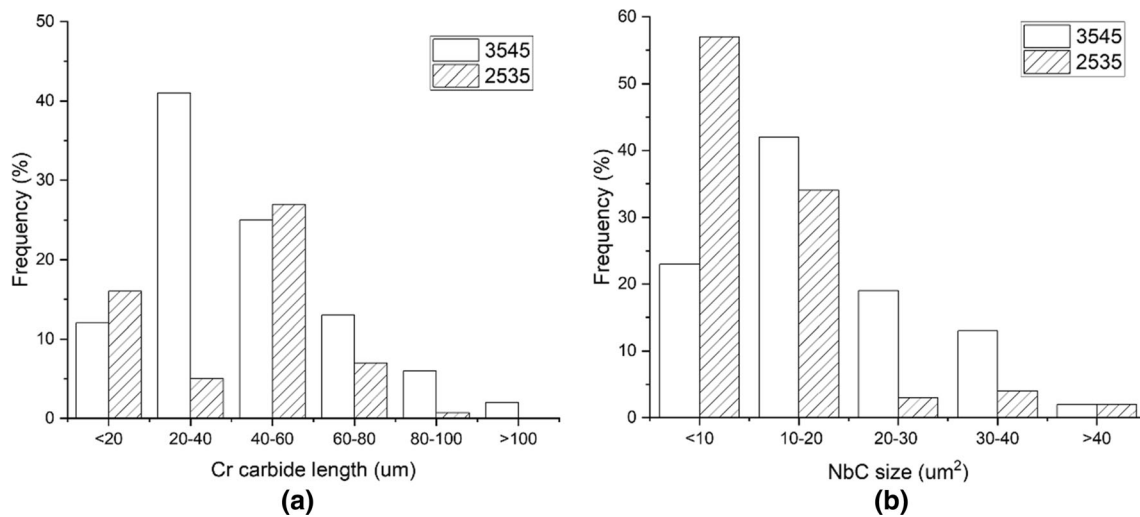

Fig. 4—The primary Cr_7C_3 carbide and Nb carbide size distribution in the microstructure of 3545 and 2535 specimens are shown in (*a*) and (*b*).

temperature decreases from 600 °C to 400 °C. In addition, the number of cycles to failure converged at a certain ratio regardless of the testing temperature for both the 2535 and 3545 specimens. The ratio for convergence is about 1.53 in 3545 specimen and 1.68 in 2535 specimen. When the applied stress amplitude results in a large ratio, the lifetime decreases as the temperature reduces. However, when lower stress ratios are applied, the number of cycles to failure decreases as

the temperature increases. The reduction in testing temperature also gradually influences the LCF behavior.

Analysis of the fatigue fracture surface provides some insight into the crack propagation behavior, and the 2535 specimens show a different fracture morphology compared with 3545 specimens. The crack initiates along the surface of the specimen, forming a thump-nail shaped crack region on the outline of fracture surface, as pointed out in Figure 9. The temperature influence on
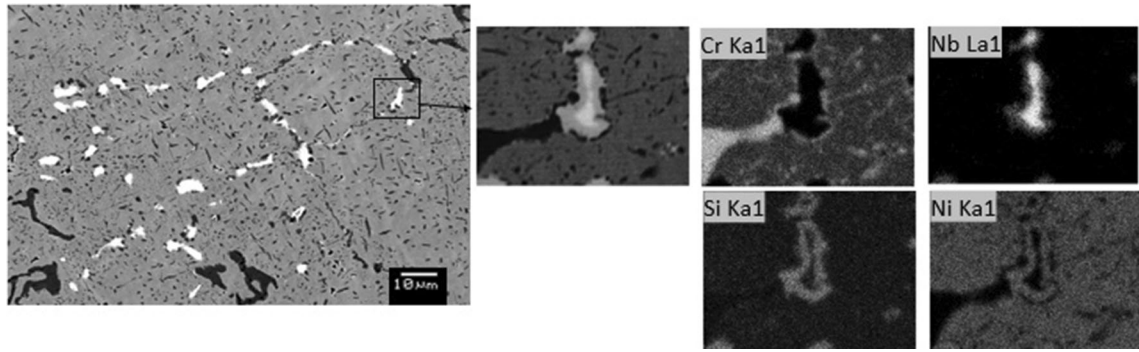
Fig. 5—The microstructure of the 3545 specimens after heat treatment. As shown in the element distribution map, the NbC transforms into Si-rich G phase. In addition, the Cr-rich precipitates were formed in the grain interior and at the grain boundary.
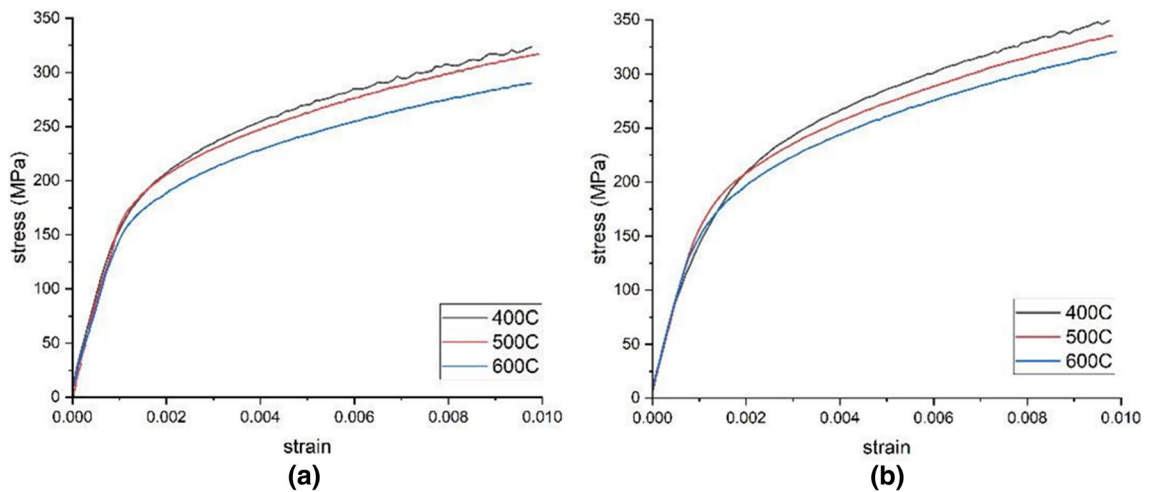

Fig. 6—The engineering stress–strain curve indicating the yield strength of (*a*) 3545 specimens and (*b*) 2535 specimens after heat treatment at various temperatures.

Table II. The Yield Strength of Cast Centralloy ET 45 MICRO (3545)[1,10] and Centralloy G 4852 MICRO (2535),[2] 3545 Specimen After Heat Treatment, 2535 Specimen After Heat Treatment

Temperature (°C)	Centralloy ET 45 MICRO[1, 10] (MPa)	Centralloy G 4852 MICRO[2] (MPa)	3545 (MPa)	2535 (MPa)
350	266	275	255*	266*
400	258	265	248	257
450	—	260	243*	253*
500	—	257	238	249
600	228	240	220	238

Values marked with * are the estimated yield strength values.

the morphology of the crack initiation site (CIS) is not obvious. Figure 10 shows the fracture surface of the fatigue test specimens for different number of cycles to failure (N_f). Both fields were picked up from the center of the fracture surface. Regardless of the N_f, a characteristic "banded" structure was apparent on the fracture surface of 3545 specimens, indicating the dendritic feature. On the other hand, in the 2535 specimens, the microstructure exhibits granular features that can be seen as marked in Figures 10(c) and (d) along with the

band-like structures on the surface. This indicates that both intergranular and transgranular fracture features exist in the 2535 specimens.

Images of the fracture surface were taken at least 20 μm away from the exterior surface and crack initiation site to eliminate the influence of stress concentration and the tearing on the matrix around the fracture surface during final fracture. The microstructure below the fracture surface was also characterized to assess the degree of damage and cracking of the primary carbides
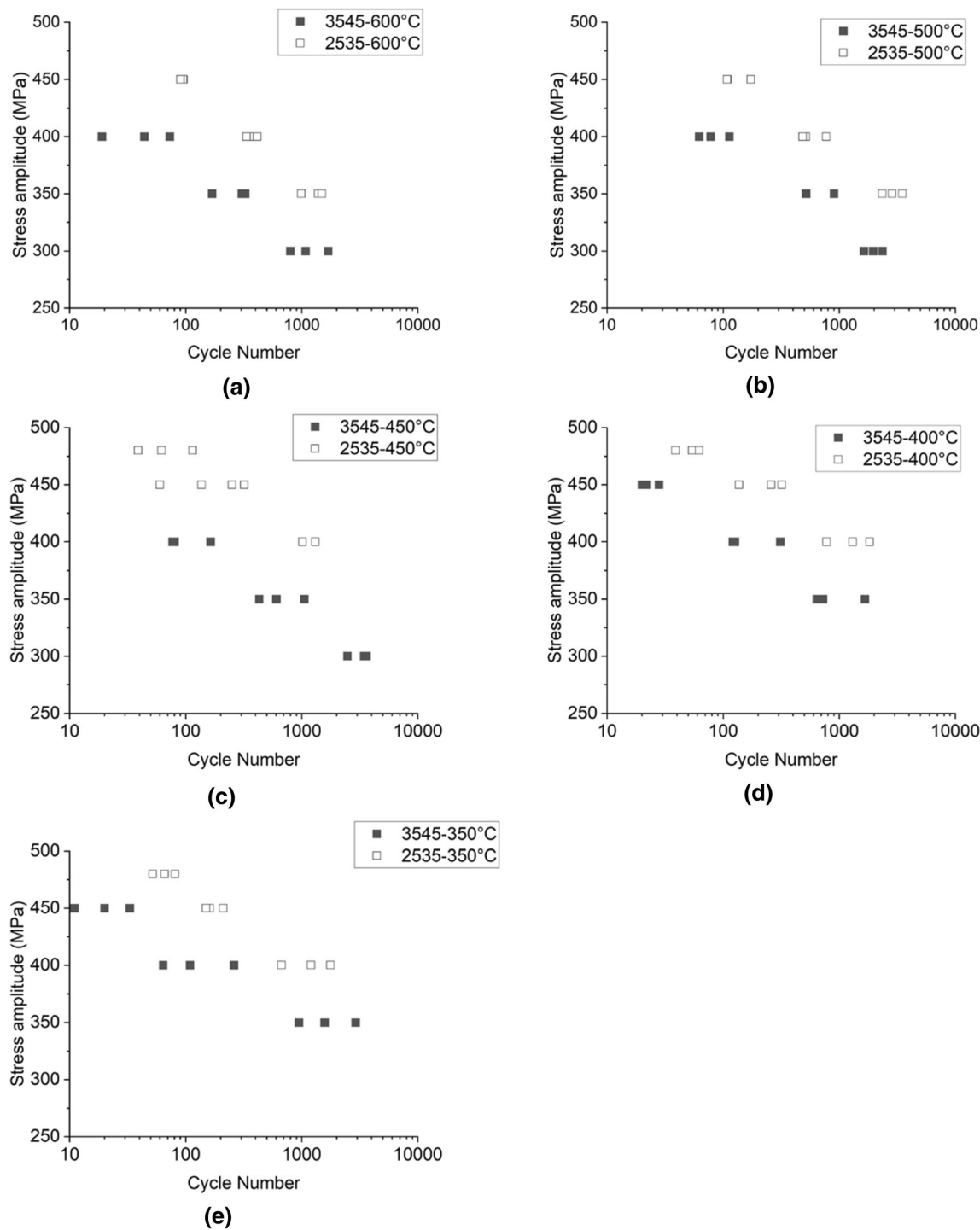
Fig. 7—Experimentally measured fatigue lives of the heat-treated 3545 and 2535 specimens at various temperatures including (*a*) 600 °C, (*b*) 500 °C, (*c*) 450 °C, (*d*) 400 °C, and (*e*) 350 °C.

during fatigue shown in Figure 11. Multiple cracks were observed to be located on the primary Cr carbides (a, c) and NbC (b, d), while the matrix interior and the secondary precipitates were absent of cracks. The planar view showing cracks appearing on individual segments of the primary Cr carbide is actually all continuous connected cracks that form throughout the carbide cluster. In addition, as shown in (d), the cracks appearing on different types of carbides can also align in a row, but are often stopped when they are adjacent and separated by long segments and patches of the matrix. This indicates that the matrix resists crack growth and serves to arrest the cracks present in the carbides. At the high stress amplitudes, the primary carbides likely serve as crack initiation sites and the
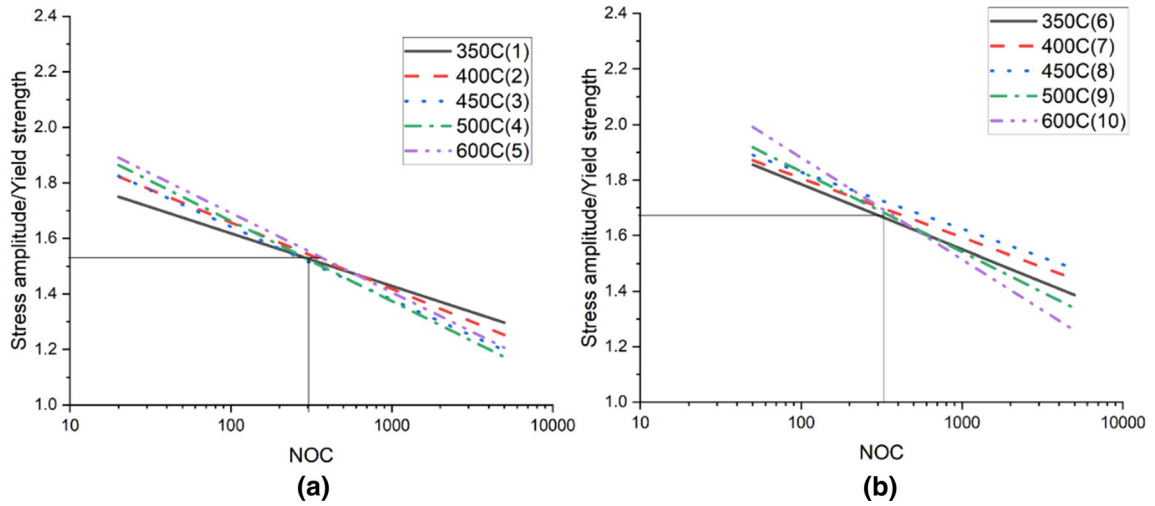
Fig. 8—The stress amplitude over yield strength versus N_f trendline of the (*a*) 3545 and (*b*) 2535 specimen at various temperatures corresponding to Table III. The results show the temperature influence on the fatigue properties of the material gradually shifts as the lifetime increases, indicating multiple crack propagation mechanism during the LCF behavior.

Table III. The Stress Amplitude Versus N_f of the 3545 and 2535 Specimen at Various Temperatures, the S^2 Represents the Coefficient of Determination

Temp./°C	3545	2535
350	(1) $\sigma_a/\sigma_Y = -0.082\ln(N_f) + 1.996$, $S^2 = 0.921$	(6) $\sigma_a/\sigma_Y = -0.101\ln(N_f) + 2.245$, $S^2 = 0.9502$
400	(2) $\sigma_a/\sigma_Y = -0.103\ln(N_f) + 2.132$, $S^2 = 0.9439$	(7) $\sigma_a/\sigma_Y = -0.093\ln(N_f) + 2.234$, $S^2 = 0.9357$
450	(3) $\sigma_a/\sigma_Y = -0.114\ln(N_f) + 2.175$, $S^2 = 0.9517$	(8) $\sigma_a/\sigma_Y = -0.089\ln(N_f) + 2.237$, $S^2 = 0.8085$
500	(4) $\sigma_a/\sigma_Y = -0.125\ln(N_f) + 2.239$, $S^2 = 0.9471$	(9) $\sigma_a/\sigma_Y = -0.126\ln(N_f) + 2.410$, $S^2 = 0.9762$
600	(5) $\sigma_a/\sigma_Y = -0.120\ln(N_f) + 2.183$, $S^2 = 0.9164$	(10) $\sigma_a/\sigma_Y = -0.159\ln(N_f) + 2.613$, $S^2 = 0.9875$

cracks are more likely to propagate in the carbide rather than matrix and secondary precipitates during the LCF.

IV. DISCUSSION

In this study, the LCF properties of HK40 type (3545) and HP40 type (2535) material after heat treatment were investigated and correlated to the microstructure. After solidification, primary Cr and NbC carbides formed within the interdendritic regions. Due to the different degree of undercooling that occurs during solidification, the grain size of the samples excised from the 3545 alloy is much larger than the 2535 alloy. In addition, despite having similar levels of carbon content in both alloy systems, the fraction and size distribution of carbides were found to vary and influence the resulting LCF properties of these alloys. The 3545 alloy was measured to possess a higher fraction of Cr carbide and lower fraction of NbC, leading to a larger size distribution of the Cr carbide clusters in the 3545 alloy. In addition, the NbC in 2535 alloy is more uniformly distributed than that in 3545 alloy. Their microstructure of the specimens after heat treatment is similar to the microstructure of the alloy observed following prolonged exposures to service temperatures.[36,37] For both alloys, the

precipitation of secondary $Cr_{23}C_6$ carbides and the transformation of NbC carbides into G phase were observed to occur within the microstructure.

The alloys investigated here are as-cast alloys, which have been aged, but are still chemically heterogeneous. The number of grains in the minimal cross-section is limited due to the cast pipe diameter. Both of these alloys were centrifugally cast into thick wall pipes from which the fatigue samples were extracted. As the grain size are not sufficient number of grains in the thickness direction in 3545 specimen to ensure continuum plasticity, multiple fatigue tests were conducted at the same conditions to evaluate reproducibility. Regardless, the grain microstructure in the center of the specimen is shown in Figures 2(e), (f). The average grain size of 3545 specimen is estimated to be over 800 μm and the grain size of 2535 specimen is about 240 μm. And the ratio of grain size over the wall thickness is over 0.1 of the 3545 specimen and 0.04 of the 2535 specimen. Applying the grain size and the primary Cr carbide size in Chan's work,[14] the crack nucleation in the experiments starts at the inclusion. Moreover, in these experiments, the minimum applied stress amplitude was over 1.4 times the yield strength in each condition, so it is highly likely that crack initiation occurred at the onset of the fatigue test.
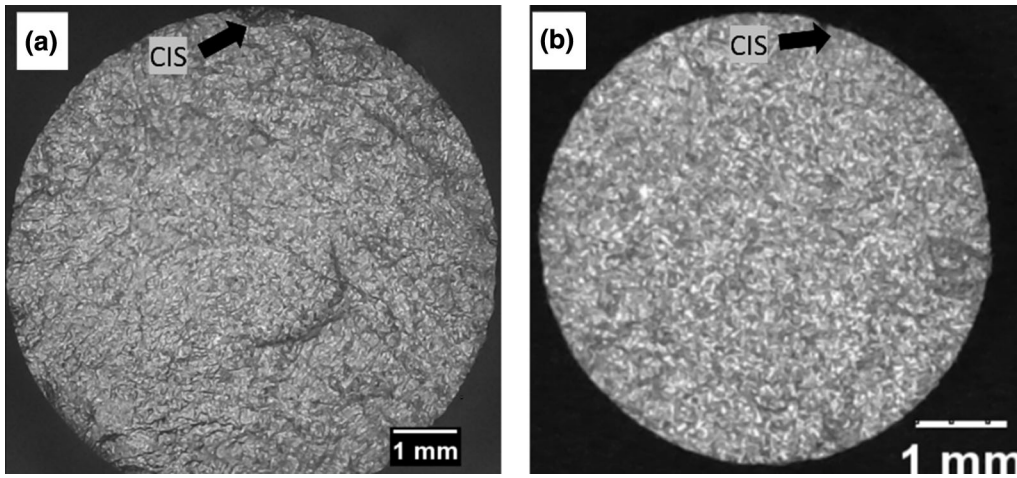
Fig. 9—The fracture surface overview of (*a*) 3545 specimen, tested at 400 MPa/400 °C, $N_f = 312$ and (*b*) 2535 specimen, tested at 450 MPa/400 °C, $N_f = 251$. The black arrow points out half-circle region on the cross-section outline, indicating the crack initiation site (CIS).
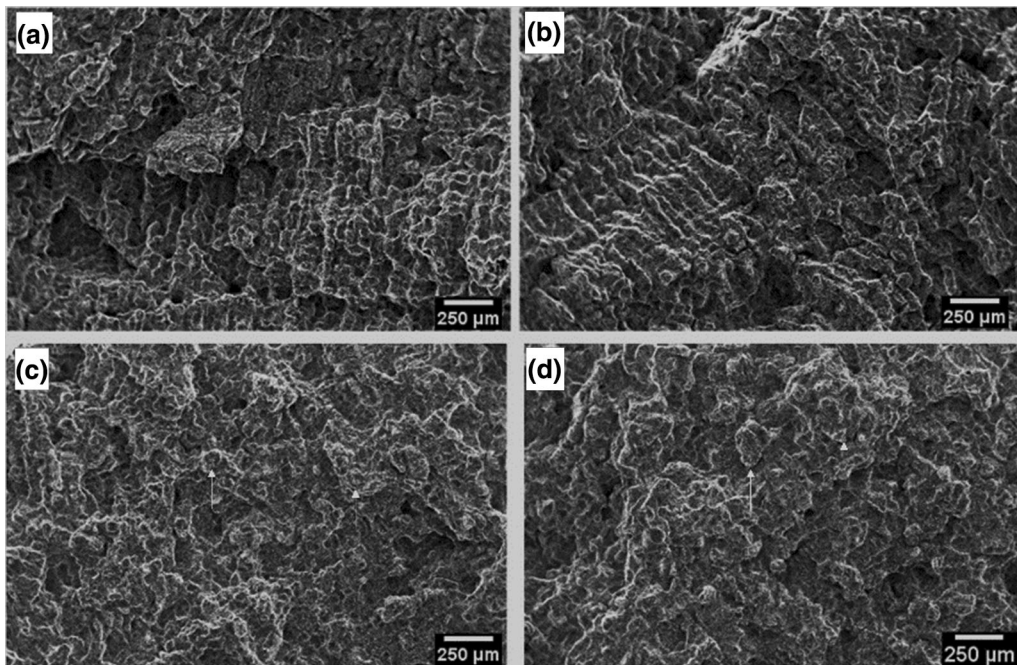

Fig. 10—The fracture surface of (*a*) 3545 specimens, tested at 450 MPa/400 °C, $N_f = 11$; (*b*) 3545 specimen, tested at 350 MPa/400 °C, $N_f = 2935$; (*c*) 2535 specimen, tested at 450 MPa/600 °C, $N_f = 90$; (*d*) 2535 specimen, tested at 350 MPa/600 °C, $N_f = 992$. The intergranular fracture can be seen in (c) and (d) as marked.

Fully reversed, stress-controlled fatigue testing revealed that the 2535 alloy shows better LCF properties than the 3545 alloy as its lifetime to failure is higher at every temperature evaluated as a part of this study. This can be rationalized by the corresponding comparison of their microstructures. From the features of the fracture surfaces shown in Figures 9, 10, and 11, it can be seen that cracks initiate and propagate through the primary carbides. It is likely that cracking of the carbides occurs as load shedding from the matrix occurs during deformation. As the matrix phase is able to plastically deform and accommodate the strain induced from the cyclic loading events, the carbides contained within the matrix are comparatively much more brittle and will fracture upon the attainment of a critical strain. Strain accumulation leads to the formation of stress concentrations that eventually promote crack propagation. Due to the slower solidification rates for the 3545 samples, the large grain sizes present in the microstructures of these samples limit the degree of resistance to crack growth when compared to the microstructure of the 2535 samples. In addition, there are minimal pores and inclusions present and they are significantly smaller than the measured particle size distributions for the carbide clusters that are located throughout the microstructure. Assessment of the fracture surface morphology also
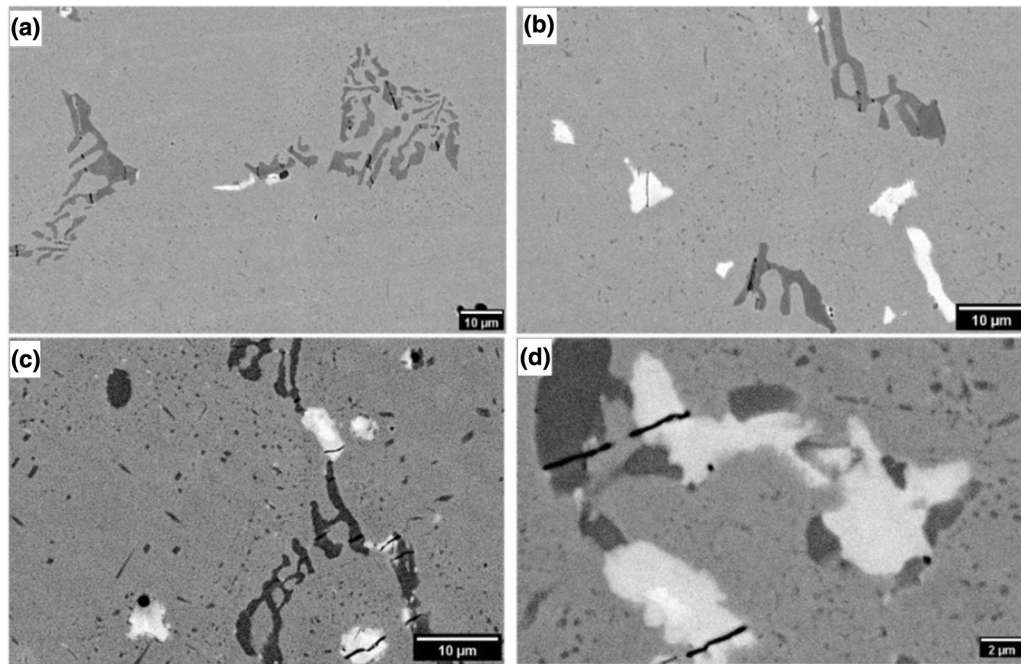
Fig. 11—The microstructure under the fracture surface of (*a*), (*b*) 3545 and (*c*), (*d*) 2535 specimen. The cracks were mostly located on the carbides. In 3545 specimens, (a) The crack on the primary Cr carbide; (b) The crack on the NbC/G phase; In 2535 specimen, (c) The crack on the primary Cr carbide; (d) The crack on the NbC/G phase.

indicates that most of the damage and fatigue cracks are located in the primary Cr carbides rather than in the matrix or on the pores. In this case, it is highly probable that the LCF properties of 3545 and 2535 alloy are mostly influenced by the grain size and the size distribution of the primary Cr carbide. Comparing the fatigue properties of 3545 with 2535, the 3545 alloy has both a larger overall grain size and a larger particle size distribution of the carbide clusters in its microstructure. Therefore, the 2535 alloy was found to exhibit better LCF properties than the 3545 alloy at same testing temperatures. As both specimens were produced by centrifugal casting, the degree of undercooling during solidification influences the nucleation and growth of grains and dendritic features[38,39] in a manner that smaller grains and the carbide clusters can be achieved. Additional improvements in the LCF properties can likely be achieved with even faster solidification rates during casting.

The yield strength of 3545 and 2535 alloy after the heat treatment did not increase significantly, as listed in Table II. The secondary precipitates are expected to impede dislocation motion in the matrix and should possess the highest effect in strengthening, but the effect of the secondary precipitates was not obvious according to the measured yield strength and the values from references. It is likely that a longer heat treatment is required to induce a higher density of secondary precipitates to form within the microstructure to effectively provide Orowan strengthening.[40] Optimization of the heat treatment might also serve to enhance the LCF fatigue properties of these alloys. The presence of a higher fraction of intergranular secondary precipitates may reduce the occurrence of stress concentrations on

the primary carbides and limit the extent of crack growth and propagation during fatigue.

The Basquin's equation[41] and Manson–Coffin's equation[32] are empirical equations that are widely used in prediction of fatigue lifetime based on stress or strain amplitude and their $N_{\rm f}$. In this investigation, the ratio of σ_a/σ_Y shows a good linear relation with the lifetime at each testing temperature for the 3545 and 2535 alloys. The model expression follows the same form as Basquin's and Manson–Coffin's equation and trendlines are shown at each temperature, as shown in (Eq. [2]). In the equation, $N_{\rm f}$ represents the lifetime to failure of the LCF test. A and C are parameters related to temperature and material. Generally, A decreases as the temperature increases. The ratio of $\frac{\sigma_a}{\sigma_Y}$ represents the maximum applied strain level in the LCF test. It should be noted that the dwell time during the test should be minimized at high temperature because creep–fatigue interactions can be significant at high temperature.[25,28] The equation may be used to provide a method in the prediction of the LCF lifetime of the HK40 type (3545) and HP40 type (2535) alloys. Compared with the LCF properties of other HK type and stainless steels,[10,41] the stress amplitude also presents an approximately linear relation with the $N_{\rm f}$.

$$\frac{\sigma_a}{\sigma_Y} = A(N_{\rm f})^C \qquad [2]$$

The influence of temperature on the LCF properties of the 3545 and 2535 alloy, shown in Figure 8, reveals that the slope of the trendline gradually increases as the temperature decreases from 600 °C to 400 °C. These results suggest that the fatigue performance is influenced

by the temperature changes after the applied strain decreases below a certain value. At stress ratios over 1.53 in the 3545 specimen and 1.68 in the 2535 specimen, the lifetime decreases when the temperature reduces. On the other hand, the lifetime increases as the temperature decreases when the ratio is lower than the converged value. This unusual behavior can likely be explained as the material is more ductile and compliant at higher temperatures, and therefore, the majority of the fatigue damage is accommodated by the matrix and limited cracking of the carbides occurs. This is consistent with the overall increase in tensile ductility of 3545 and 2535 specimen observed as a function of temperature.[42,43] As temperatures decrease, the fatigue properties increase once the ratio becomes lower than the converged value. This is likely attributed to creep–fatigue interactions. At high temperatures, creep and stress relaxation can serve to reduce the magnitude of internal stresses incurred during cyclic loading. The ability of the material to relax the elastic stresses decreases as the temperature reduces. For stress-controlled fatigue, the macro-scale stress relaxation and cyclic hardening and softening can be effectively eliminated above a certain temperature. The degree of damage created by fatigue and creep is not independent. As the overall testing duration increases at elevated temperature, environmental effects and microstructural changes can also occur to modify the resultant fatigue behavior. There are multiple assessment methods of creep-fatigue lifetime, such as life fraction rule[44] and strain range partitioning,[45] but it requires independent measurements to evaluate the degree of damage in pure fatigue and creep conditions. To summarize, testing durations associated with a high stress amplitude tend to be short and the increased temperature can improve the ductility and damage tolerance of material, leading to better LCF resistance. At lower stress amplitudes that result in longer testing durations and time at elevated temperature, the fatigue performance at higher temperatures tends to be worse as the cumulative effects of environmental damage and creep–fatigue interactions temperature become dominant and trigger failure.

In summary, this investigation studied the LCF properties of centrifugal cast HK40 type (3545) and HP40 type (2535) alloys. Under stress-controlled testing, the HP40 alloy shows better resistance to LCF than HK40 due to its refined grain size and smaller particle size distribution of primary Cr carbides. Microstructural observations revealed that cracks are more likely to propagate through the primary carbides rather than in the matrix or on the secondary precipitates. At high stress amplitudes, elevated temperatures improve the ductility, thereby improving the fatigue properties. However, for lower stress amplitudes where the test durations are prolonged, creep–fatigue interactions and environmental damage occur at elevated temperature, leading to a reduction in the fatigue life of the alloys.

V. CONCLUSION

From the current study, the low cycle fatigue properties of centrifugal casting Centralloy ET 45 MICRO (3545) and Centralloy G 4852 MICRO (2535) at elevated temperatures were investigated. The fatigue results are presented as a function of the stress amplitude versus lifetime. The influence of microstructure and temperature on the LCF properties at elevated temperature was also discussed. Based on the experimental results, the following conclusions can be reached:

1. In the cast microstructure, more Cr carbides and less NbC were present in 3545 than the 2535 alloy. Primary Cr carbides reside within the interdendritic regions and form a cluster shape. The Cr carbide clusters in 3545 alloy are larger than the ones in the 2535 alloy. The grain size in 3545 alloy was also larger than 2535 alloy due to different solidification conditions. After heat treatment, secondary Cr carbides precipitate within the matrix and G phase are formed from the original NbC due to the Ni and Si diffusion.
2. The stress amplitude versus N_f plots show the LCF properties of the materials. The ratio of stress amplitude over yield strength $\frac{\sigma_a}{\sigma_Y}$ was used to fit log functions with N_f. The LCF properties of 3545 specimens studied in this investigation were more prone to fatigue failure at elevated temperatures than the 2535 specimen.
3. Large clusters of primary Cr carbides likely serve as initiation sites for LCF fatigue damage. The increased range of the particle size distribution for primary Cr carbide clusters is likely responsible for the reduced fatigue resistance of the 3545 alloy when compared with the 2535 alloy.
4. The elevated temperature can improve the ductility but also promote the creep-fatigue effect. A high temperature improves the LCF properties with large stress amplitude but deteriorate it with small stress amplitude.

CONFLICT OF INTEREST

On behalf of all authors, the corresponding author states that there is no conflict of interest.

REFERENCES

1. Material datasheet, Centralloy ET 45 MICRO, efaidnbmnnnibpca-jpcglclefindmkaj/https://www.schmidt-clemens.de/fileadmin/scdownloads/werkstoffdatenblaetter/WST_ET_45_micro_161109.pdf.
2. Material datasheet, Centralloy G 4852 MICRO, efaidnbmnnnibpcajpcglclefindmkaj/https://www.schmidt-clemens.com/fileadmin/sc-downloads/werkstoffdatenblaetter/WST_4852_Micro_161109.pdf.
3. W.Z. Wang, F.Z. Xuan, Z.D. Wang, B. Wang, and C.J. Liu: *Mater. Des.*, 2011, vol. 32, pp. 4010–16.
4. B. Piekarski: *Mater. Charact.*, 2001, vol. 47, pp. 181–86.
5. C.-M. Fuyang, J.-Y. Chen, B. Shao, Y. Zhou, J.-M. Gong, X.-F. Guo, and Y. Jiang: *Int. J. Press. Vessels Pip.*, 2021, vol. 192, p. 104391.
6. R.C. Ecob, R.C. Lobb, and V.L. Kohler: *J. Mater. Sci.*, 1987, vol. 22, pp. 2867–80.
7. M. Abbasi, I. Park, Y. Ro, Y. Ji, R. Ayer, and J.-H. Shim: *Mater. Charact.*, 2019, vol. 148, pp. 297–306.
8. N. Vaché, P. Steyer, C. Duret-Thual, M. Perez, T. Douillard, E. Rauch, and M. Véron: *Materialia*, 2020, vol. 9, p. 100593.
9. A.A. Kaya, P. Krauklis, and D.J. Young: *Mater. Charact.*, 2002, vol. 49, pp. 11–21.
10. Y.-J. Kim, D.-G. Lee, H.K. Jeong, Y.-T. Lee, and H. Jang: *Mater. Eng. Perform.*, 2010, vol. 19, pp. 700–04.
11. M. Ekström and S. Jonsson: *Mater. Sci. Eng. A*, 2014, vol. 616, pp. 78–87.
12. N.E. Frost, K.J. Marsh, and L.P. Pook: *Metal Fatigue*, Courier Corporation, North Chelmsford, 1999.
13. M.D. Sangid: *Int. J. Fatigue*, 2013, vol. 57, pp. 58–72.
14. K.S. Chan: *Int. J. Fatigue*, 2010, vol. 32, pp. 1428–47.
15. K. Kobayashi, K. Yamaguchi, M. Hayakawa, and M. Kimura: *Mater. Lett.*, 2015, vol. 59, pp. 383–86.
16. D. Gopikrishna, S.N. Jha, and L.N. Dash: *Superalloys*, 1997, vol. 718, pp. 625–706.
17. A.R. Balachandramurthi, J. Moverare, N. Dixit, and R. Pederson: *Mater. Sci. Eng. A*, 2018, vol. 735, pp. 463–74.
18. Y. Nadot, J. Mendez, and N. Ranganathan: *Int. J. Fatigue*, 2004, vol. 26, pp. 311–19.
19. S. Vantadori, C. Ronchei, D. Scorza, A. Zanichelli, and R. Luciano: *Fatigue Fract. Eng. Mater. Struct.*, 2022, vol. 45, pp. 2734–47.
20. K.S. Chan: *Metall. Mater. Trans. A*, 2020, vol. 51A, pp. 1148–162.
21. M. Kamaya: *Int. J. Fatigue*, 2013, vol. 55, pp. 102–11.
22. K. Kobayashi, K. Yamaguchi, M. Hayakawa, and M. Kimura: *Int. J. Fatigue*, 2008, vol. 30, pp. 1978–84.
23. R.P. Skelton, ed.: *High Temperature Fatigue: Properties and Prediction*, Springer Science & Business Media, Berlin, 2012.
24. M.S.J. Hashmi: *Comprehensive Materials Processing*, Newnes, Oxford, 2014.
25. C. Cabet, L. Carroll, and R. Wright: *J. Press. Vessel Technol.*, 2013. https://doi.org/10.1115/1.4025080.
26. S. Konosu: *Fatigue Fract. Eng. Mater. Struct.*, 1994, vol. 17, pp. 683–93.
27. L. Sun, X.-G. Bao, S.-J. Guo, R.-Z. Wang, X.-C. Zhang, and S.-T. Tu: *Int. J. Fatigue*, 2021, vol. 147, p. 106187.
28. M. Sauzay, M. Mottot, L. Allais, M. Noblecourt, I. Monnet, and J. Périnet: *Nucl. Eng. Des.*, 2004, vol. 232, pp. 219–36.
29. A. Saxena and S.J. Hudak: *Fract. Mech. ASTM STP*, 1979, vol. 677, pp. 215–32.
30. Y.J. Oh, J.H. Hong, and S.W. Nam: *Metall. Mater. Trans. A*, 2000, vol. 31A, pp. 1761–75.
31. J.L. Bassani and F.A. McClintock: *Int. J. Solids Struct.*, 1981, vol. 17, pp. 479–92.
32. P.P. Gillis: *Acta Metall.*, 1966, vol. 14, pp. 1673–76.
33. G.V. Prasad Reddy, P.M. Dinesh, R. Sandhya, K. Laha, and T. Jayakumar: *Int. J. Fatigue*, 2016, vol. 92, pp. 272–80.
34. B. Zhang, R. Wang, D. Hu, K. Jiang, J. Mao, F. Jing, and X. Hao: *Chin. J. Aeronaut.*, 2021, vol. 34, pp. 112–21.
35. M.L. Saucedo-Muñoz, A. Ortiz-Mariscal, V.M. Lopez-Hirata, J.D. Villegas-Cardenas, O. Soriano-Vargas, and E.O. Avila-Davila: *Int. J. Miner. Metall. Mater.*, 2017, vol. 24, pp. 1125–33.
36. M. Roussel, X. Sauvage, M. Perez, D. Magné, A. Hauet, A. Steckmeyer, M. Vermont, T. Chaise, and M. Couvrat: *Materialia*, 2018, vol. 4, pp. 331–39.
37. P.G. Caceres-Valencia and I.J. Baiges: *J. Fail. Anal. Prev.*, 2006, vol. 6, pp. 67–72.
38. S. Mohapatra, H. Sarangi, and U.K. Mohanty: *Manuf. Rev.*, 2020, vol. 7, p. 26.
39. N.S. Madhusudhan and G.C. Mohan Kumar: *Int. J. Sci. Eng. Res.*, 2012, vol. 3, pp. 1–3.
40. G. Monnet: *Philos. Mag.*, 2006, vol. 86, pp. 5927–41.
41. W. Hwang and K.S. Han: *J. Compos. Mater.*, 1986, vol. 20, pp. 154–65.
42. C.-K. Lin, P.-K. Lai, and T.-S. Shih: *Int. J. Fatigue*, 1996, vol. 18, pp. 297–307.
43. S. Leuders, T. Lieneke, S. Lammers, T. Tröster, and T. Niendorf: *J. Mater. Res.*, 2014, vol. 29, pp. 1911–19.
44. S. Konosu, T. Koshimizu, T. Iijima, and K. Maeda: *J. Mech. Des.*, 1993, vol. 115, no. 1, pp. 41–6. https://doi.org/10.1115/1.2919322.
45. S.S. Manson: *Int. Symp. Fatigue Elev. Temp.*, No. NASA-TM-X-68171, 1972.